MATERIALS SCIENCE

Atomic-scale imaging of ytterbium ions in lead halide perovskites

Wen Xu[1], Jiamu Liu[2], Bin Dong[1]*, Jindou Huang[1], Honglong Shi[3], Xiangxin Xue[2], Mao Liu[2]*

Lanthanide-doped lead halide perovskites have demonstrated great potential for photoelectric applications. However, there is a long-standing controversy about the existence of lanthanide ions, e.g., whether the doping of Ln^{3+} is successful or not; the substituting sites of Ln^{3+} in lead halide perovskites are unclear. We directly identify the doped Yb^{3+} in $CsPbCl_3$ perovskites by using the state-of-the-art transmission electron microscopy and three-dimensional atom probe tomography at atomic scale. Different from the previous assumptions and/or results, we evidence that Yb^{3+} simultaneously replace Pb^{2+} and occupy the lattice interstitial sites. Furthermore, we directly observe the cluster phenomenon of $CsPbCl_3$ single crystal at near atomic scale. Density functional theory modeling further confirms and explains the mechanisms of our findings. Our findings thus provide an atomic-level understanding of the doping mechanism in perovskites and will stimulate a further thinking of the doping effect on the performance of perovskites.

INTRODUCTION

Metal halide perovskites have been emerged as the flourishing materials owing to their facile synthesis, high absorption coefficients, defect tolerance, tunable bandgaps, superior charge-transfer properties, etc. (*1–7*). As a representative perovskite, lead halide perovskites process the typical crystal structure with the chemical formula of ABX_3, where A represents a monovalent inorganic or organic cation [$MA^+ = CH_3NH_3^+$; $FA^+ = HC(NH_2)_2^+$; or Cs^+], B presents Pb^{2+}, and X is a halide anion (typically, Cl^-, Br^-, I^-, or mixtures thereof) (*8, 9*). The great achievements based on lead halide perovskites in photovoltaics and optoelectronics have been made, such as solar cells (*10–12*), light-emitting diodes (LEDs) (*13–15*), photodetectors (*16–18*), and lasers (*19*). However, pristine perovskites have some inherent drawbacks, for instance, limited adjustability of optical and electrical properties and poor stability (against water, oxygen, heat, etc.).

Impurity doping is a promising strategy to expand properties and to simulate applications of perovskite materials (*20–23*). Lanthanide ions are endowed with the rich energy levels of $4f^n$, sharp emission lines, long decay lifetimes, and broad emission range spanning from ultraviolet to near-infrared region and flexible redox properties (*24, 25*). Therefore, various lanthanide ions ($Ln^{3+/2+}$: Ce^{3+}, Pr^{3+}, Nd^{3+}, Sm^{3+}, Eu^{3+}/Eu^{2+}, Gd^{3+}, Tb^{3+}, Dy^{3+}, Ho^{3+}, Er^{3+}, Tm^{3+}, Yb^{3+}/Yb^{2+}, etc.) have been incorporated into perovskites to notably improve their performances and broaden their applications via single-, co-, or tri-doping, respectively (*26–33*). Many landmark works have been achieved by the marriage of lanthanide ions with perovskites. For example, dual band emissions originating from excitons and Ln^{3+} in Ln^{3+}-doped perovskite nanocrystals (e.g., $CsPbX_3$) with the greatly broadened spectral range of 1600 nm were observed, realizing the first single-component

electroluminescent white perovksite LEDs (*34, 35*). The highly efficient quantum cutting of Yb^{3+} in the near-infrared (photoluminescent quantum efficiency of 190%) was found sensitized by the $CsPb(Cl_{1-x}Br_x)_3$ host nanocrystals, which was used to largely boost the efficiency of commercial silicon solar cells (*28, 36*). The long-term durability of perovskite solar cells was notably improved by incorporating europium ion pair $Eu^{3+}-Eu^{2+}$ in perovskite film to selectively oxidize Pb^0 and reduce I^0 defects (*37*). Moreover, the perovskites with reduced defects, enhanced carrier transport, improved ultraviolet stability, decreased grain boundary and increased grain sizes, altered bandgap, adjusted morphology, etc., were also widely reported by inducing lanthanide ions (*38–40*).

Despite these great advances, there have been continuously controversies about lanthanide ion–doped perovskites since the first discovery in 2017 (*35*). Considering the differences of valence states and ions radius for lanthanide ions with the ions in perovskites (e.g., Pb^{2+}) and low crystallization temperature of perovskites, now, the main debates include whether the doping of Ln^{3+} is successful or not, or the substituting sites of Ln^{3+} in $APbX_3$ are unclear, whether occupying the sites of Pb^{2+}, the lattice interstitial sites, and/or the surface of perovskite (*28, 31, 40, 41*). A number of reports speculated that the Ln^{3+} possibly replaces Pb^{2+} at B sites by first-principles calculation and x-ray photoelectron spectroscopy technique (*35, 38, 42*), while some of them concluded that lanthanide ions may be on the surface of perovskites (*37, 43*). Ascertaining these debates is vital to reveal the mechanisms behind the impressive performance of lanthanide ion–doped perovskites. Whereas, it is yet to be fully understood, lacking of direct evidence of lanthanide ions in perovskites.

Although the highly beam-sensitive nature of perovskites makes high-resolution electron microscopy extremely challenging (*44–47*), aberration-corrected atomic-resolution scanning transmission electron microscopy (AC-STEM) and three-dimensional (3D) atom probe tomography (APT) tests were used to directly observe the doped ytterbium ions in the crystal lattice of $CsPbCl_3$ perovskites at atomic scale in this study, which clarified the aforementioned argument. In addition, APT tests were used to discover the cluster phenomenon of lead halide perovskites. The in-depth doping

[1]Key Laboratory of New Energy and Rare Earth Resource Utilization of State Ethnic Affairs Commission, School of Physics and Materials Engineering, Dalian Minzu University, 18 Liaohe West Road, Dalian 116600, P. R. China. [2]School of Metallurgy, Northeastern University, Shenyang 110819, China. [3]School of Science, Minzu University of China, Beijing, China.
*Corresponding author. Email: dong@dlnu.edu.cn (B.D.); liumao@mail.neu.edu.cn (M.L.)

mechanism has been revealed and explained by both experimental observations and density functional theory (DFT) modeling.

RESULTS AND DISCUSSION

First, the most representative rare earth ion–doped perovskite nanocrystals, $CsPbCl_3:Yb^{3+}$, were synthesized through the modified hot injection method (fig. S1; see the "Methods" section) (28), which demonstrates cubic shape with the diameter of ~20 nm (fig. S2, A to C). The high-resolution x-ray diffraction in fig. S3 reveals that the unit cell volume of $CsPbCl_3$ decreases after Yb^{3+} doping, which would be caused by the substitution of Pb^{2+} (1.8 Å) with small atomic radius of Yb^{3+} (~1.75 Å). Considering the highly beam-sensitive nature of perovskites (44, 47), perovskite nanocrystals doped with Yb^{3+} are characterized by low-dose AC-STEM high-angle annular dark-field (HAADF) imaging operated at 120 kV with a screen current of ~20 pA (see the "Methods" section). It is one of the low-dose techniques that have been used for other materials to produce less damage with the same total electron fluence (dose) (44–47), to obtain their atomic-scale images. Figure 1 (A and B) shows the atomically resolved HAADF images of the $CsPbCl_3$ nanocrystals doped with Yb^{3+} and the corresponding atomic structures, which demonstrate a perfect cubic perovskite structure projected along the perovskite <100> direction (35). As revealed in Fig. 1B, because of the large difference in atomic numbers Z between Cs ($Z = 55$) and Pb ($Z = 82$), the individual atomic columns associated with Cs and Pb can be clearly distinguished according to the apparent image intensity, which are indicated by blue and yellow dots, respectively. The pure chlorine columns ($Z = 17$) can also be identified (cyan dots) however are less clearly visible in the HAADF image. The Fourier transformation further confirms the presence of the {010} and {100} planes in $CsPbCl_3:Yb^{3+}$ perovskite

nanocrystals (Fig. 1C and fig. S2D), which are often missing from atomic-resolution studies of beam-damaged perovskites. Therefore, it is evident from Fig. 1 that the perfect cubic crystal structure of perovskites (Fig. 1D) is successfully captured by AC-STEM.

Figure 2 displays the atomic-resolution HAADF-STEM and energy-dispersive x-ray spectroscopy (EDS) mapping images of the $CsPbCl_3:Yb^{3+}$ perovskite nanocrystals. As presented in Fig. 2 (B to E), the elements of Pb, Cs, Cl, and Yb are clearly identified in $CsPbCl_3:Yb^{3+}$, which are further evidenced by STEM-EDS mapping in fig. S4. It demonstrates that the Yb^{3+} are successfully doped into the $CsPbCl_3$ nanocrystals. Figure 2 (F to H) exhibits the merged mapping images of $Yb^{3+}-Pb^{2+}$, $Yb^{3+}-Cs^+$, and Cs^+-

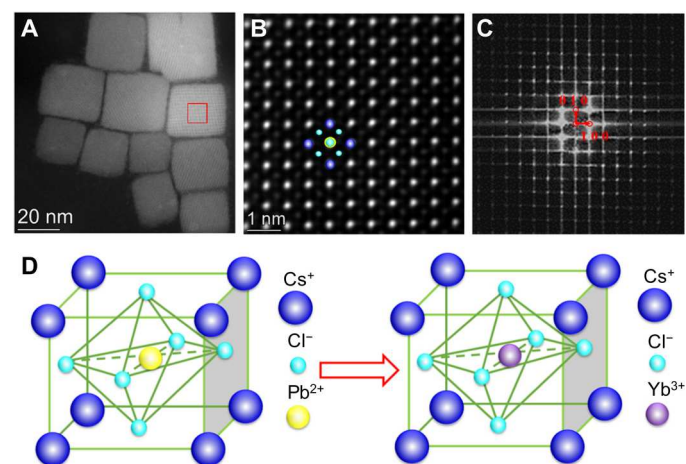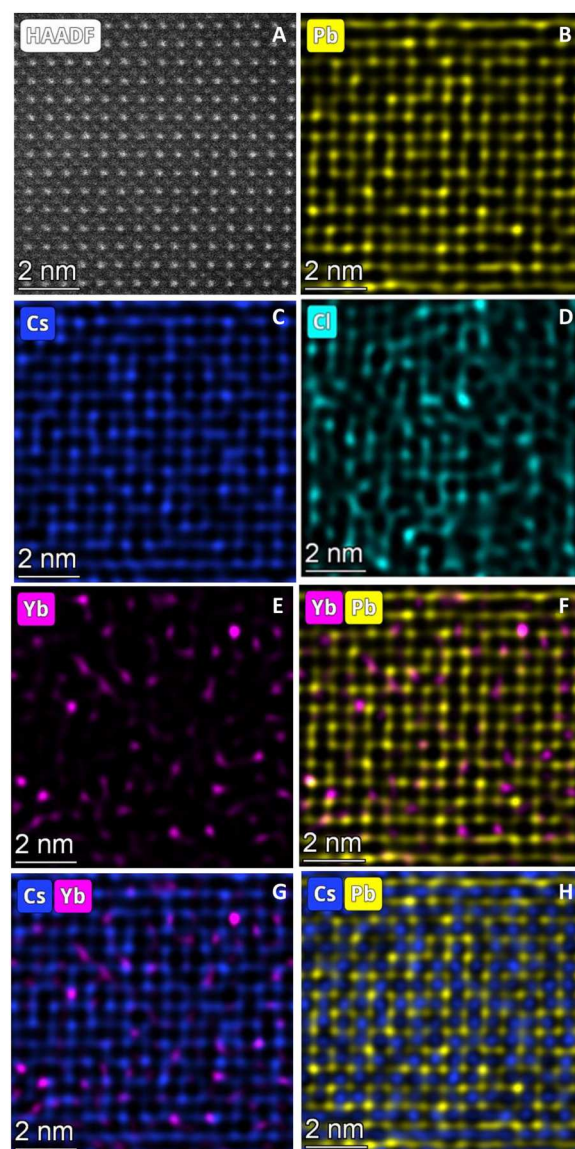**Fig. 1. Atomic-resolution imaging of the $CsPbCl_3:Yb^{3+}$ perovskite structure.** (**A**) General morphology of $CsPbCl_3$ nanocrystals doped with Yb ions. (**B**) Atomic-resolution HAADF-STEM micrograph of the magnified region highlighted by a red square in (A) showing a high contrast for the Cs and Pb sites, with a poor Cl contrast. The overlapped yellow and cyan balls show the Pb/Cl (or Yb/Cl) column, the cyan balls show the pure Cl columns, and the blue balls show the Cs columns. (**C**) The Fourier transformation confirms the presence of the {010} and {100} planes. The screen current used for image acquisition in (A) and (B) is ~20 pA. (**D**) The atomic unit cell represented by the balls in (B). It also shows that Pb ion is replaced by Yb ion.

Fig. 2. Atomic-resolution HAADF-STEM and EDS mapping images of the $CsPbCl_3:Yb^{3+}$ perovskite nanocrystals. (**A**) HAADF-STEM image of the magnified region highlighted by a red square in Fig. 1A. (**B to E**) Atomic-resolution EDS maps of the magnified region highlighted by a red square in Fig. 1A, representing Pb, Cs, Cl, and Yb, respectively. (**F to H**) Comparisons of EDS maps of Yb and Pb, Yb and Cs, and Pb and Cs, respectively.

Pb^{2+}, respectively. Incredibly, Fig. 2F reveals that Yb^{3+} not only are incorporated into the $CsPbCl_3$ but also partially simultaneously replace Pb^{2+} and occupy the lattice interstitial sites in the crystal. The typical sites in lattice for the replaced Pb^{2+} are marked by green circles, while the occupied lattice interstitial sites are marked by blue circles. In addition, the intensity profiles for these two types are provided, as displayed in fig. S5. In addition, there is a little chance that Cs^+ can be replaced by Yb^{3+}, as displayed in Fig. 2G. Cs^+ and Pb^{2+} are completely independent in their proper position (Fig. 2H). The drift will inevitably occur when conducting the HAADF-STEM and EDS mapping measurement, which may influence our results. As can be seen in Fig. 2 (F to H), the atoms on the edge of the mappings look connected together. However, in most areas of mapping images (Fig. 2H), the atoms of Cs^+-Pb^{2+} are right where they belong. In addition, the atomic-resolution HAADF-STEM and EDS mapping images of the pristine $CsPbCl_3$ perovskite nanocrystals (fig. S6) further evidence that such low-dose characterization techniques can directly image Yb^{3+} doped in lead halide perovskites at atomic scale. Our observations are completely different from the previous speculation or experimental results, e.g., on the surface of perovskite, only replacing Pb^{2+}, or hard to dope (28, 37, 41). It provides the direct evidence at atomic scale that Yb^{3+} can be doped into the $CsPbCl_3$ nanocrystals by simultaneously replacing Pb^{2+} and occupying the lattice interstitial sites, which solve the long-time dispute regarding the rare earth ions doping into lead halide perovskites (31, 43). The rare earth ions (e.g., Yb^{3+}) were tried to dope into various semiconductors (31), such as ZnS and CdSe, and only the excellent optical performance in the system of Yb^{3+}-doped perovskites was obtained. The doping mechanism for both the replaced Pb^{2+} and occupied lattice interstitial sites of Yb ions may associate with high-performance of perovskite after rare earth ion doping, for example, the closer distance among Yb^{3+} in crystals, realizing the highly efficient quantum cutting from perovskite to Yb^{3+} (48).

To further comprehend the doping mechanism in perovskites, a $CsPbCl_3$:Yb^{3+} perovskite single crystal with the diameter of ~500 mm was successfully prepared through the modified hydrothermal method (49), as characterized in fig. S7. APT tests can provide the 3D elemental information inside the materials at near atomic scale (50, 51). 3D elemental maps based on APT were used to visualize atom distribution in the $CsPbCl_3$:Yb^{3+} perovskite single crystal, to check whether there is an obvious nonuniformity in its microstructures. Quantitative investigation on elemental distribution in the $CsPbCl_3$:Yb^{3+} perovskite single crystal can be achieved by performing statistical analysis on APT datasets including 1D concentration analysis, k-nearest neighbor distance analysis, and frequency distribution analysis (50). The APT needle with the tip less than 100 nm was obtained using focused ion beam technique (fig. S8), which was nailed into the inside of $CsPbCl_3$:Yb^{3+} perovskite single crystal for mapping the elements with the size of 17 nm by 17 nm by 40 nm. 3D elemental mapping in Fig. 3A presents that the Cs, Cl, and Yb ions homogeneously distribute in the $CsPbCl_3$ crystal, further providing overwhelming evidence of the successful doping of Yb^{3+}. It is noteworthy that the apparent segregation of the Pb elements exists in the individual atom maps of the $CsPbCl_3$:Yb^{3+} perovskite single crystal. Figure 3B gives 1D concentration profiles along a cylindrical region with a diameter of 5 nm in APT reconstructions of the $CsPbCl_3$:Yb^{3+} perovskite single crystal. It clearly demonstrates the uniform doping of Yb ions and the substantial concentration

fluctuation of Pb element (Fig. 3A and fig. S9). The concentration value of Yb^{3+} is around ~5%, which is smaller than that of the precursor concentration in the synthesis process. Figure 3C shows the frequency distribution analysis of all the elements based on APT data. In general, experimental frequency distribution should be consistent with the hypothesized binomial distribution. However, the frequency distributions will broaden compared to the binomial distribution expected if clustering occurs (51, 52), like the Pb cluster. Previous studies revealed that the Pb cluster at nanoscale existed at the boundary of perovskite grains (53). Our observations prove the doping of Yb^{3+} and, meanwhile, found the Pb cluster at near atomic scale even in perovskite single crystals. It is crucial to understand the stability mechanism of perovskites.

To further investigate the Yb^{3+} doping mechanism, DFT (54, 55) was performed to calculate the Yb formation energies (E_{form}) in three cases, as displayed in the optimized geometry structures of possible interstitial and substitutional configurations of Yb^{3+} in $CsPbCl_3$ (Fig. 4, A to C): substituting Pb atom with Yb atom on the Pb site (S_{Yb}-$CsPbCl_3$), occupying the lattice interstitial sites with Yb atom (I_{Yb}-$CsPbCl_3$), or simultaneously substituting Pb atom and occupying the lattice interstitial sites with Yb atoms (S_{Yb}-I_{Yb}-$CsPbCl_3$), respectively. The calculation results show that the energy of S_{Yb}-$CsPbCl_3$ is ~0.21 eV, lower than the energy of undoped $CsPbCl_3$. As a comparison, the formation energy of I_{Yb}-$CsPbCl_3$ is ~0.15 eV, which indicates that Yb atoms entering interstitial sites are thermodynamically instable. When Yb atoms coexist in the substitutional sites and interstitial sites, the energy of S_{Yb}-I_{Yb}-$CsPbCl_3$ is about 3.33 eV, which is much larger than that of $CsPbCl_3$, suggesting that Yb atoms entering the substitutional and interstitial sites simultaneously are the most favorable thermodynamically. It is entirely consistent with the experimental results (Fig. 2).

As illustrated in Fig. 4 (A to C), the Yb occupying the substitutional sites can form six Yb—Cl bonds with the neighboring Cl, which is similar with the case of S_{Yb}-$CsPbCl_3$, and the Yb occupying interstitial sites can form six Yb—Cl bonds and one Yb—Cs bond with neighboring Cl and Cs, respectively, as can also be seen in the case of I_{Yb}-$CsPbCl_3$. Besides, we can see that Yb-Yb distance in the S_{Yb}-I_{Yb}-$CsPbCl_3$ system is about 3.675 Å, slightly short than the Yb—Yb bond length (3.723 Å) in Yb metal, which suggests that Yb—Yb bonds can be formed in the S_{Yb}-I_{Yb}-$CsPbCl_3$ system. These Yb—Yb bonds well explain the low energy and high thermodynamic stability of S_{Yb}-I_{Yb}-$CsPbCl_3$. Furthermore, we optimized the geometry structures of the S_{Yb}-$CsPbCl_3$ (010) surfaces with different Cl defects, as shown in Fig. 4 (D and E). The energy calculations show that the formation energy of Cl defects near Pb is 0.84 eV lower than the formation energy of Cl defects near Yb. Thus, it can be concluded that the Cl defects are mainly distributed nearby Pb. As a result, the exposed Pb acts as the adsorption active center, and the chemical stability of $CsPbCl_3$ decreases with the increase of Cl defects. Therefore, the partial substitution of Yb for Pb in $CsPbCl_3$ improves the formation energy of Cl defects, which is beneficial for reducing Cl defects and increases the chemical stability of $CsPbCl_3$ (28, 56). These coincide to the experimental stability improvement of perovskites, demonstrating the great potential for improving the long-term stability, including the air and light stability by rare earth ion doping.

Here, we synthesized the Yb^{3+}-doped $CsPbCl_3$ perovskite nanocrystals and crystals through the modified hot injection method and
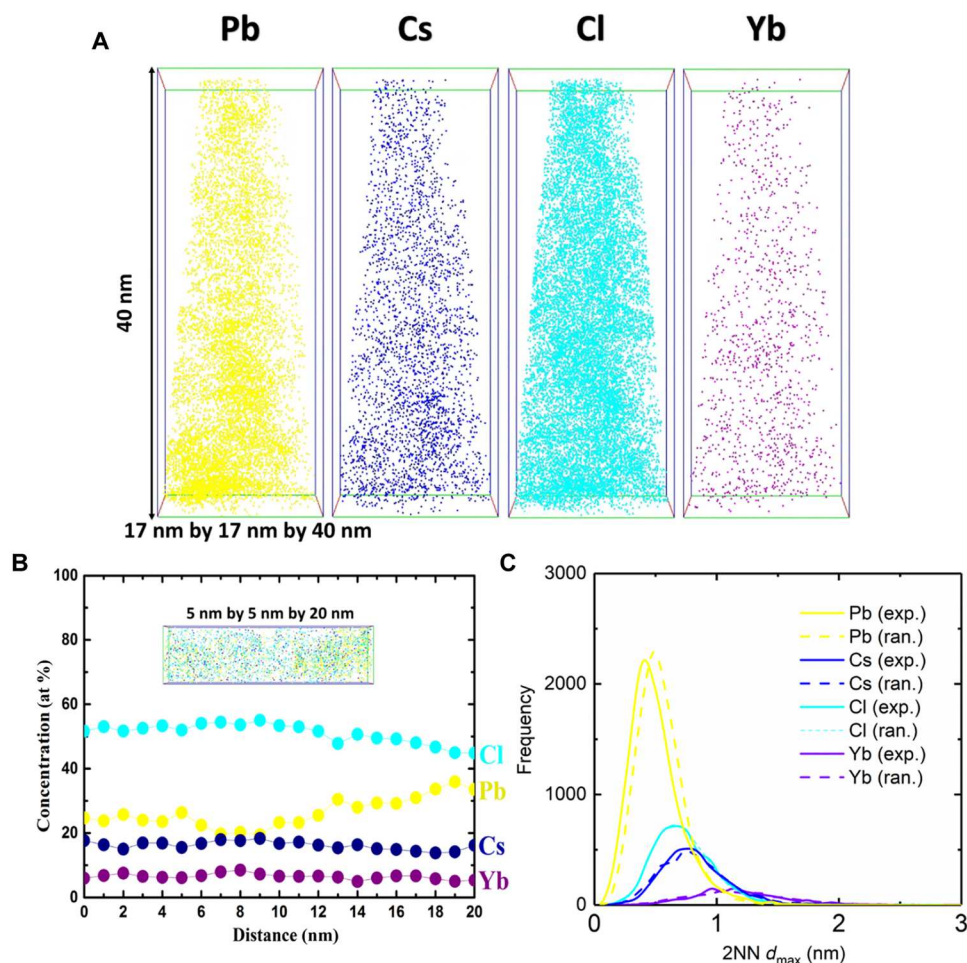
Fig. 3. APT characterization of CsPbCl$_3$:Yb^{3+} perovskite single crystal. (**A**) Atom maps of Pb, Cs, Cl, and Yb. (**B**) 1D concentration profile (with 1-nm bin width) taken along the cylinder (of 5-nm diameter, as shown in the inset). at %, atomic %. (**C**) K-nearest neighbor distance analysis ($k = 2$). 2NN, K-nearest neighbor.

hydrothermal method. Then, the Yb^{3+} in CsPbCl$_3$ at atomic scale was directly imaged using the state-of-the-art transmission electron microscopy and 3D APT. We experimentally and theoretically evidenced that Yb^{3+} simultaneously replace Pb^{2+} and occupy the lattice interstitial sites. Our findings broke the long-standing debate on the doping mechanism of rare earth ions in lead halide perovskites and will offer a deep understanding and further development of doped perovskites.

MATERIALS AND METHODS
Materials
Hydrochloric acid solution (HCl, 37 wt% in H$_2$O) was obtained from Sinopharm Chemical Reagent Beijing Co., Ltd.), CsCl, Pb(CH$_3$COO)$_2$·3H$_2$O (99.5%), PbCl$_2$·6H$_2$O (99.5%), and isopropyl alcohol (C$_8$H$_8$O, 99.5%) were purchased from Macklin. Oleamine, oleic acid, octadecene, YbCl$_3$·6H$_2$O (99.9%), Yb (CH$_3$COO)$_3$·4H$_2$O (99.9%), and acetone (≥99.5%) were purchased from Sigma-Aldrich. All chemicals were used as received without any further purification.

Methods
Synthesis of Yb^{3+} doped CsPbCl$_3$ nanocrystals
Yb^{3+}-doped CsPbCl$_3$ perovskite nanocrystals were synthesized by the modified hot injection method (*28*). Firstly, YbCl$_3$ (0.1 mmol) was adequately dissolved into 10 ml ODE at 160°C for 1 hour under purging N$_2$ gas. Then, lead halide (0.4 mmol), OAm (1 ml), OA (1 ml) were continued heated at 160°C for 1 hour. After the complete dissolution of YbCl$_3$ and PbCl$_2$, the temperature was raised to 240°C under purging N$_2$ gas. After that, the as-prepared Cs- oleate (0.8 ml) was swiftly injected and after 30 s the solution was immediately cooled with an ice bath. The Yb^{3+} doped CsPbCl$_3$ nanocrystals were precipitated with acetone and centrifuged followed by dissolution in toluene.

Fabrication of Yb^{3+} doped CsPbCl$_3$ single crystals
The CsPbCl$_3$:Yb^{3+} single crystals were fabricated by the modified method in previous literature (*48*). Firstly, 1.0 g Pb(CH$_3$COO)$_2$·3H$_2$O and 0.15 g Yb (CH$_3$COO)$_3$·4H$_2$O were completed dispersed in 10 ml HCl. Then, a mixed solution containing 0.40 g CsCl and 2 ml HCl was added into the above solution, and stirred overnight at 60°C forming a clear solution. Subsequently, the mixture was transferred to a reaction kettle, and was placed in the
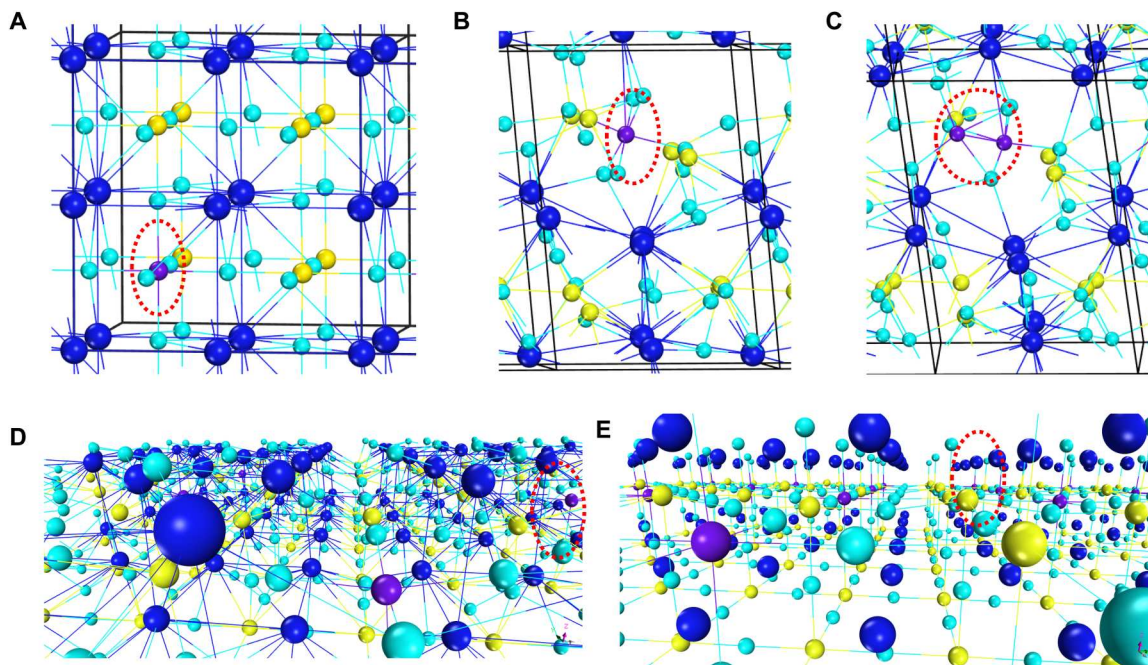
Fig. 4. Calculated structure of CsPbCl₃:Yb³⁺ perovskites. Structures of S_{Yb}-CsPbCl₃ (**A**), I_{Yb}-CsPbCl₃ (**B**), S_{Yb}-I_{Yb}-CsPbCl₃ (**C**), S_{Yb}-CsPbCl₃ (101) surfaces with Cl defects near Yb (**D**), and S_{Yb}-CsPbCl₃ (101) surfaces with Cl defects near Pb (**E**); yellow, purple, blue, and cyan spheres represent the Pb, Yb, Cs, and Cl atoms, respectively.

oven at 240°C for 20 hours. After that, the reaction was cooled to room temperature at 3°C/h, and the product was collected by washed with isopropyl alcohol 2 to 3 times. Finally, the CsPbCl₃:Yb³⁺ single crystals were dried at 60°C in a vacuum oven for 24 hours before use.

XRD and XPS characterization
Powder x-ray diffraction (XRD) patterns were recorded by using a Rigaku TTRIII x-ray diffractometer at 200 mA and 40 kV with Cu Kα radiation (λ = 1.5406 Å). The x-ray photoelectron spectroscopy (XPS) was performed on the Kratos Axis Ultra DLD spectrometer equipped with a monochrome Al Kα x-ray source (hν = 1486.6 eV), which was operated by a drive power of 150 W with a multichannel plate and a delay line detector under 1.0×10^{-9} Torr vacuum.

STEM HAADF imaging and EDS characterization
Firstly, the Yb³⁺-doped CsPbCl₃ perovskite nanocrystals were deposited on the carbon-coated side of copper TEM grids for further use, and were loaded rapidly into the microscope. Microscopy for imaging and condition development was performed on two microscopes. HAADF imaging was performed by an aberration-corrected Thermofisher Themis Z (60 to 300 kV) scanning transmission electron microscope (operated at 120 KV with a screen current of 20 pA) to capture the atomic structure of CsPbCl₃:Yb³⁺ nanocrystals. This TEM is equipped with a DCOR⁺ aberration corrector and a field emission gun (X-FEG) with monochromator. The inner and outer collection angles for the STEM images were 38 and 200 mrad, respectively, with a semi convergence angle of 28 mrad. Atomic resolution EDS mapping was acquired in the STEM mode with a ChemiSTEM technology (X-FEG and SuperX EDS with four windowless silicon drift detectors) operated at 120 kV with a screen current of 50 pA. To reduce electron beam induced damage to the perovskite NCs, all alignments and focusing were done away from the areas for imaging.

Atom Probe Tomography (APT) characterization
The APT sample was prepared in a CsPbCl₃ single crystal by using Focused Ion Beam (FIB) milling (Thermofisher Scios 2). It was thinned down to ~40 nm in diameter at an accelerating voltage of 30 kV with a current decreasing from 0.2 nA to 50 pA, followed by a final polish at an accelerating voltage of 5 kV with an extremely low current of 10 pA to remove the surface amorphous layer. The data acquisition was carried out in a CAMECA LEAP 5000X under ultrahigh vacuum of approximately 2.5×10^{-11} torr, at a specimen temperature of 80 K. The CAMECA integrated visualization and analysis software IVAS 3.8.4 was used for data processing and three-dimensional atomic reconstruction.

DFT simulation
All theoretical researches in this work are completed using the density functional theory (DFT) in Cambridge Serial Total Energy Package (CASTEP) (53). We employ Perdew-Burke-Ernzerhof (PBE) correlation functional in Generalized Gradient Approximation (GGA) to exchange related energy (54). In the calculation, the cut-off energy is set as 600 eV; the convergence tolerance for energy was set as 1×10^{-6} eV/atom; and the tolerance for maximum force was 0.03 eV/Å. A (2×2×2) supercell was employed to simulate these substitutional and interstitial doping CsPbCl₃ systems, and the calculations for the formation energy of surface Cl defect are performed in a (1×1) surface supercell containing 4 layers of an CsPbCl₃ slab showing (010) facets and ~15 Å vacuum.

To determine relative stability of different configurations of the Yb occupying interstitial or subsituational sites, we calculated the Yb formation energies (E_{form}) in the following three cases:

a) CsPbCl₃ substituting Yb atom for Pb atom on the Pb site (S_{Yb}-CsPbCl₃) $E_{form} = E(S_{Yb}\text{-}CsPbCl_3) + \mu_{Pb} - E(CsPbCl_3) - \mu_{Yb}$

b) CsPbCl₃ with Yb atom entering interstitial site of (I_{Yb}-CsPbCl₃) $E_{form} = E(I_{Yb}\text{-}CsPbCl_3) - E(CsPbCl_3) - \mu_{Yb}$

c) CsPbCl$_3$ with Yb atoms coexisting in substitutional sites and interstitial sites (S$_{Yb}$-I$_{Yb}$-CsPbCl$_3$) E$_{form}$ = E(S$_{Yb}$-I$_{Yb}$-CsPbCl$_3$) + μ$_{Pb}$ − E(CsPbCl$_3$) − 2 × μ$_{Yb}$

where, E(S$_{Yb}$-CsPbCl$_3$), E(I$_{Yb}$-CsPbCl$_3$), and E(S$_{Yb}$-I$_{Yb}$-CsPbCl$_3$) are the total energy of the Yb-doped CsPbCl$_3$ systems; E(CsPbCl$_3$) is the total energy of the pure CsPbCl$_3$; μ$_{Pb}$ and μ$_{Yb}$ are the chemical potential of Pb and Yb, respectively.

Supplementary Materials

This PDF file includes:
Figs. S1 to S9

REFERENCES AND NOTES

1. L. M. Herz, Charge-carrier mobilities in metal halide perovskites: Fundamental mechanisms and limits. *ACS Energy Lett.* **2**, 1539–1548 (2017).

2. X.-K. Liu, W. Xu, S. Bai, Y. Jin, J. Wang, R. H. Friend, F. Gao, Metal halide perovskites for light-emitting diodes. *Nat. Mater.* **20**, 10–21 (2021).

3. D. P. McMeekin, G. Sadoughi, W. Rehman, G. E. Eperon, M. Saliba, M. T. Hörantner, A. Haghighirad, N. Sakai, L. Korte, B. Rech, M. B. Johnston, L. M. Herz, H. J. Snaith, A mixed-cation lead mixed-halide perovskite absorber for tandem solar cells. *Science* **351**, 151–155 (2016).

4. Z. Ni, H. Jiao, C. Fei, H. Gu, S. Xu, Z. Yu, G. Yang, Y. Deng, Q. Jiang, Y. Liu, Y. Yan, J. Huang, Evolution of defects during the degradation of metal halide perovskite solar cells under reverse bias and illumination. *Nat. Energy* **7**, 65–73 (2022).

5. S. D. Stranks, H. J. Snaith, Metal-halide perovskites for photovoltaic and light-emitting devices. *Nat. Nanotechnol.* **10**, 391–402 (2015).

6. W. Zhang, G. E. Eperon, H. J. Snaith, Metal halide perovskites for energy applications. *Nat. Energy* **1**, 16048 (2016).

7. Y. Lei, Y. Li, C. Lu, Q. Yan, Y. Wu, F. Babbe, H. Gong, S. Zhang, J. Zhou, R. Wang, R. Zhang, Y. Chen, H. Tsai, Y. Gu, H. Hu, Y. H. Lo, W. Nie, T. Lee, J. Luo, K. Yang, K. I. Jang, S. Xu, Perovskite superlattices with efficient carrier dynamics. *Nature* **608**, 317–323 (2022).

8. M. T. Klug, A. Osherov, A. A. Haghighirad, S. D. Stranks, P. R. Brown, S. Bai, J. T. W. Wang, X. Dang, V. Bulović, H. J. Snaith, A. M. Belcher, Tailoring metal halide perovskites through metal substitution: Influence on photovoltaic and material properties. *Energ. Environ. Sci.* **10**, 236–246 (2017).

9. C. Yi, J. Luo, S. Meloni, A. Boziki, N. Ashari-Astani, C. Grätzel, S. M. Zakeeruddin, U. Röthlisberger, M. Grätzel, Entropic stabilization of mixed A-cation ABX$_3$ metal halide perovskites for high performance perovskite solar cells. *Energ. Environ. Sci.* **9**, 656–662 (2016).

10. Y. Zhao, I. Yavuz, M. Wang, M. H. Weber, M. Xu, J. H. Lee, S. Tan, T. Huang, D. Meng, R. Wang, J. Xue, S. J. Lee, S. H. Bae, A. Zhang, S. G. Choi, Y. Yin, J. Liu, T. H. Han, Y. Shi, H. Ma, W. Yang, Q. Xing, Y. Zhou, P. Shi, S. Wang, E. Zhang, J. Bian, X. Pan, N. G. Park, W. Lee, Y. Yang, Suppressing ion migration in metal halide perovskite via interstitial doping with a trace amount of multivalent cations. *Nat. Mater.* **21**, 1396–1402 (2022).

11. G. Yang, Z. Ni, Z. J. Yu, B. W. Larson, Z. Yu, B. Chen, A. Alasfour, X. Xiao, J. M. Luther, Z. C. Holman, J. Huang, Defect engineering in wide-bandgap perovskites for efficient perovskite–silicon tandem solar cells. *Nat. Photonics* **16**, 588–594 (2022).

12. R. Lin, J. Xu, M. Wei, Y. Wang, Z. Qin, Z. Liu, J. Wu, K. Xiao, B. Chen, S. M. Park, G. Chen, H. R. Atapattu, K. R. Graham, J. Xu, J. Zhu, L. Li, C. Zhang, E. H. Sargent, H. Tan, All-perovskite tandem solar cells with improved grain surface passivation. *Nature* **603**, 73–78 (2022).

13. Y.-H. Kim, J. Park, S. Kim, J. S. Kim, H. Xu, S. H. Jeong, B. Hu, T. W. Lee, Exploiting the full advantages of colloidal perovskite nanocrystals for large-area efficient light-emitting diodes. *Nat. Nanotechnol.* **17**, 590–597 (2022).

14. A. Fakharuddin, M. K. Gangishetty, M. Abdi-Jalebi, S. H. Chin, A. R. bin Mohd Yusoff, D. N. Congreve, W. Tress, F. Deschler, M. Vasilopoulou, H. J. Bolink, Perovskite light-emitting diodes. *Nat. Electron.* **5**, 203–216 (2022).

15. X. Meng, S. Ji, Q. Wang, X. Wang, T. Bai, R. Zhang, B. Yang, Y. Li, Z. Shao, J. Jiang, K. L. Han, F. Liu, Organic–inorganic hybrid cuprous-based metal halides for warm white light-emitting diodes. *Adv. Sci.* **9**, 2203596 (2022).

16. J. Feng, C. Gong, H. Gao, W. Wen, Y. Gong, X. Jiang, B. Zhang, Y. Wu, Y. Wu, H. Fu, L. Jiang, X. Zhang, Single-crystalline layered metal-halide perovskite nanowires for ultrasensitive photodetectors. *Nat. Electron.* **1**, 404–410 (2018).

17. J. Jiang, M. Xiong, K. Fan, C. Bao, D. Xin, Z. Pan, L. Fei, H. Huang, L. Zhou, K. Yao, X. Zheng, L. Shen, F. Gao, Synergistic strain engineering of perovskite single crystals for highly stable and sensitive X-ray detectors with low-bias imaging and monitoring. *Nat. Photonics* **16**, 575–581 (2022).

18. Q. Lin, "Metal halide perovskites for photodetection," in *Photoconductivity and Photoconductive Materials: Fundamentals, Techniques and Applications*, vol. 2 (Wiley, 2022), pp. 781–805.

19. H. Dong, C. Zhang, X. Liu, J. Yao, Y. S. Zhao, Materials chemistry and engineering in metal halide perovskite lasers. *Chem. Soc. Rev.* **49**, 951–982 (2020).

20. C.-H. Lu, G. V. Biesold-McGee, Y. Liu, Z. Kang, Z. Lin, Doping and ion substitution in colloidal metal halide perovskite nanocrystals. *Chem. Soc. Rev.* **49**, 4953–5007 (2020).

21. Y. Lin, Y. Shao, J. Dai, T. Li, Y. Liu, X. Dai, X. Xiao, Y. Deng, A. Gruverman, X. C. Zeng, J. Huang, Metallic surface doping of metal halide perovskites. *Nat. Commun.* **12**, 7 (2021).

22. J. Euvrard, Y. Yan, D. B. Mitzi, Electrical doping in halide perovskites. *Nat. Rev. Mater.* **6**, 531–549 (2021).

23. T. Liu, X. Zhao, J. Li, Z. Liu, F. Liscio, S. Milita, B. C. Schroeder, O. Fenwick, Enhanced control of self-doping in halide perovskites for improved thermoelectric performance. *Nat. Commun.* **10**, 5750 (2019).

24. J.-C. G. Bünzli, C. Piguet, Taking advantage of luminescent lanthanide ions. *Chem. Soc. Rev.* **34**, 1048–1077 (2005).

25. B. Zhou, B. Shi, D. Jin, X. Liu, Controlling upconversion nanocrystals for emerging applications. *Nat. Nanotechnol.* **10**, 924–936 (2015).

26. W. J. Mir, T. Sheikh, H. Arfin, Z. Xia, A. Nag, Lanthanide doping in metal halide perovskite nanocrystals: Spectral shifting, quantum cutting and optoelectronic applications. *NPG Asia Mater.* **12**, 9 (2020).

27. R. Sun, D. Zhou, Y. Ding, Y. Wang, Y. Wang, X. Zhuang, S. Liu, N. Ding, T. Wang, W. Xu, H. Song, Efficient single-component white light emitting diodes enabled by lanthanide ions doped lead halide perovskites via controlling Förster energy transfer and specific defect clearance. *Light Sci. Appl.* **11**, 340 (2022).

28. G. Pan, X. Bai, D. Yang, X. Chen, P. Jing, S. Qu, L. Zhang, D. Zhou, J. Zhu, W. Xu, B. Dong, H. Song, Doping lanthanide into perovskite nanocrystals: Highly improved and expanded optical properties. *Nano Lett.* **17**, 8005–8011 (2017).

29. J. Sun, W. Zheng, P. Huang, M. Zhang, W. Zhang, Z. Deng, S. Yu, M. Jin, X. Chen, Efficient near-infrared luminescence in lanthanide-doped vacancy-ordered double perovskite Cs$_2$ZrCl$_6$ phosphors via Te^{4+} sensitization. *Angew. Chem.* **61**, e202201993 (2022).

30. L. Zhang, M. Yuan, Lanthanide doped lead-free double perovskites as the promising next generation ultra-broadband light sources. *Light Sci. Appl.* **11**, 99 (2022).

31. R. Marin, D. Jaque, Doping lanthanide ions in colloidal semiconductor nanocrystals for brighter photoluminescence. *Chem. Rev.* **121**, 1425–1462 (2021).

32. Y. Liu, X. Rong, M. Li, M. S. Molokeev, J. Zhao, Z. Xia, Incorporating rare-earth terbium(III) ions into Cs2AgInCl6:Bi nanocrystals toward tunable photoluminescence. *Angew. Chem. Int. Ed.* **59**, 11634–11640 (2020).

33. X. Luo, T. Ding, X. Liu, Y. Liu, K. Wu, Quantum-cutting luminescent solar concentrators using ytterbium-doped perovskite nanocrystals. *Nano Lett.* **19**, 338–341 (2019).

34. R. Sun, P. Lu, D. Zhou, W. Xu, N. Ding, H. Shao, Y. Zhang, D. Li, N. Wang, X. Zhuang, B. Dong, X. Bai, H. Song, Samarium-doped metal halide perovskite nanocrystals for single-component electroluminescent white light-emitting diodes. *ACS Energy Lett.* **5**, 2131–2139 (2020).

35. D. Zhou, D. Liu, G. Pan, X. Chen, D. Li, W. Xu, X. Bai, H. Song, Cerium and ytterbium codoped halide perovskite quantum dots: A novel and efficient downconverter for improving the performance of silicon solar cells. *Adv. Mater.* **29**, 1704149 (2017).

36. D. M. Kroupa, J. Y. Roh, T. J. Milstein, S. E. Creutz, D. R. Gamelin, Quantum-cutting ytterbium-doped CsPb(Cl$_{1−x}$Br$_x$)$_3$ perovskite thin films with photoluminescence quantum yields over 190%. *ACS Energy Lett.* **3**, 2390–2395 (2018).

37. L. Wang, H. Zhou, J. Hu, B. Huang, M. Sun, B. Dong, G. Zheng, Y. Huang, Y. Chen, L. Li, Z. Xu, N. Li, Z. Liu, Q. Chen, L. D. Sun, C. H. Yan, A Eu^{3+}-Eu^{2+} ion redox shuttle imparts operational durability to Pb-I perovskite solar cells. *Science* **363**, 265–270 (2019).

38. J. Duan, Y. Zhao, X. Yang, Y. Wang, B. He, Q. Tang, Lanthanide ions doped CsPbBr$_3$ halides for HTM-free 10.14%-efficiency inorganic perovskite solar cell with an ultrahigh open-circuit voltage of 1.594 V. *Adv. Energy Mater.* **8**, 1802346 (2018).

39. Z. Song, W. Xu, Y. Wu, S. Liu, W. Bi, X. Chen, H. Song, Incorporating of lanthanides ions into perovskite film for efficient and stable perovskite solar cells. *Small* **16**, 2001770 (2020).

40. Y. Xie, B. Peng, I. Bravić, Y. Yu, Y. Dong, R. Liang, Q. Ou, B. Monserrat, S. Zhang, Highly efficient blue-emitting CsPbBr$_3$ perovskite nanocrystals through neodymium doping. *Adv. Sci.* **7**, 2001698 (2020).

41. J. Y. D. Roh, M. D. Smith, M. J. Crane, D. Biner, T. J. Milstein, K. W. Krämer, D. R. Gamelin, Yb^{3+} speciation and energy-transfer dynamics in quantum-cutting Yb^{3+}-doped CsPbCl$_3$ perovskite nanocrystals and single crystals. *Phys. Rev. Mater.* **4**, 105405 (2020).

42. T. J. Milstein, D. M. Kroupa, D. R. Gamelin, Picosecond quantum cutting generates photoluminescence quantum yields over 100% in ytterbium-doped CsPbCl$_3$ nanocrystals. *Nano Lett.* **18**, 3792–3799 (2018).

43. Z. Zeng, Y. Xu, Z. Zhang, Z. Gao, M. Luo, Z. Yin, C. Zhang, J. Xu, B. Huang, F. Luo, Y. Du, C. Yan, Rare-earth-containing perovskite nanomaterials: Design, synthesis, properties and applications. *Chem. Soc. Rev.* **49**, 1109–1143 (2020).

44. M. U. Rothmann, J. S. Kim, J. Borchert, K. B. Lohmann, C. M. O'Leary, A. A. Sheader, L. Clark, H. J. Snaith, M. B. Johnston, P. D. Nellist, L. M. Herz, Atomic-scale microstructure of metal halide perovskite. *Science* **370**, eabb5940 (2020).

45. Y. Yu, D. Zhang, C. Kisielowski, L. Dou, N. Kornienko, Y. Bekenstein, A. B. Wong, A. P. Alivisatos, P. Yang, Atomic resolution imaging of halide perovskites. *Nano Lett.* **16**, 7530–7535 (2016).

46. K. Song, L. Liu, D. Zhang, M. P. Hautzinger, S. Jin, Y. Han, Atomic-resolution imaging of halide perovskites using electron microscopy. *Adv. Energy Mater.* **10**, 1904006 (2020).

47. Y. Zhou, H. Sternlicht, N. P. Padture, Transmission electron microscopy of halide perovskite materials and devices. *Joule* **3**, 641–661 (2019).

48. X. Li, S. Duan, H. Liu, G. Chen, Y. Luo, H. Ågren, Mechanism for the extremely efficient sensitization of Yb^{3+} luminescence in $CsPbCl_3$ nanocrystals. *J. Phys. Chem. Lett.* **10**, 487–492 (2019).

49. L. Zi, W. Xu, R. Sun, Z. Li, J. Zhang, L. Liu, N. Wang, Y. Wang, N. Ding, J. Hu, S. Y. Lu, H. Zhu, H. Song, Lanthanide-doped $MAPbI_3$ single crystals: Fabrication, optical and electrical properties, and multi-mode photodetection. *Chem. Mater.* **34**, 7412–7423 (2022).

50. R. Hu, S. Jin, G. Sha, Application of atom probe tomography in understanding high entropy alloys: 3D local chemical compositions in atomic scale analysis. *Prog. Mater. Sci.* **123**, 100854 (2022).

51. Y. Yu, C. Zhou, S. Zhang, M. Zhu, M. Wuttig, C. Scheu, D. Raabe, G. J. Snyder, B. Gault, O. Cojocaru-Mirédin, Revealing nano-chemistry at lattice defects in thermoelectric materials using atom probe tomography. *Mater. Today* **32**, 260–274 (2020).

52. M. Miller, R. Forbes, *Atom-Probe Tomography: The Local Electrode Atom Probe* (Springer, 2014).

53. A. Alberti, C. Bongiorno, E. Smecca, I. Deretzis, A. La Magna, C. Spinella, Pb clustering and PbI_2 nanofragmentation during methylammonium lead iodide perovskite degradation. *Nat. Commun.* **10**, 2196 (2019).

54. K. Capelle, E. Gross, Spin-density functionals from current-density functional theory and vice versa: A road towards new approximations. *Phys. Rev. Lett.* **78**, 1872–1875 (1997).

55. B. Hammer, L. B. Hansen, J. K. Nørskov, Improved adsorption energetics within density functional theory using revised Perdew-Burke-Ernzerhof functionals. *Phys. Rev. B* **59**, 7413–7421 (1999).

56. E. Akman, T. Ozturk, W. Xiang, F. Sadegh, D. Prochowicz, M. M. Tavakoli, P. Yadav, M. Yilmaz, S. Akin, The effect of B-site doping in all-inorganic $CsPbI_xBr_{3−x}$ absorbers on the performance and stability of perovskite photovoltaics. *Energ. Environ. Sci.* **16**, 372–403 (2023).

Science Advances

Atomic-scale imaging of ytterbium ions in lead halide perovskites

Wen Xu, Jiamu Liu, Bin Dong, Jindou Huang, Honglong Shi, Xiangxin Xue, and Mao Liu

View the article online
https://www.science.org/doi/10.1126/sciadv.adi7931
Permissions
https://www.science.org/help/reprints-and-permissions

Use of this article is subject to the Terms of service